

RIS-aided Positioning Experiments based on mmWave Indoor Channel Measurements

Moustafa Rahal^{*‡}, Benoît Denis^{*}, Taghrid Mazloum^{*}, Frederic Munoz^{*}, and Raffaele D’Errico^{*}

^{*}CEA-Leti, Université Grenoble Alpes, F-38000 Grenoble, France

[‡]Université Rennes 1, IETR - UMR 6164, F-35000 Rennes, France

Abstract—Reconfigurable Intelligent Surfaces (RISs) are announced as a truly transformative technology, capable of smartly shaping wireless environments to optimize next generation communication networks. Among their numerous foreseen applications, Reflective RISs (RRISs) have been shown theoretically beneficial not only to enable wireless localization through controlled multipath in situations where conventional systems would fail (e.g., with too few available base stations (BSs) and/or under radio blockages) but also to locally boost accuracy on demand (typically, in regions close to the surface). In this paper, leveraging a dedicated frequency-domain mmWave indoor channel sounding campaign, we present the first experimental evidences of such benefits, by emulating offline simple RIS-aided single-BS positioning scenarios including line-of-sight (LoS) and non-line-of-sight (NLoS), single-RIS and multi-RIS, and multiple user equipment (UE) locations, also by considering various combinations of estimated multipath parameters (e.g., delays, Angle of Departure (AoD) or gains) as inputs to basic Least Squares (LS) solvers. Despite their simplicity, these preliminary proof-of-concept validations show concretely how and when RIS-reflected paths could contribute to enhance localization performance.

Index Terms—Indoor Channel Sounding, Multipath Parameters, NLoS, Proof-of-Concept Validations, Reconfigurable Intelligent Surface, Vector Network Analyzer, Wireless Localization.

I. INTRODUCTION

RISs, which consist of controllable nearly-passive devices behaving as electromagnetic mirrors or lenses, are foreseen as an enabling breakthrough technology for beyond fifth generation (B5G) wireless systems [1], [2]. These surfaces can purposely modify the wireless propagation environments to optimize communication networks in the sense of improved Quality of Service (QoS), extended coverage, low power consumption, limited field exposure [3], and more. Regarding wireless localization, RISs have been shown not only to locally boost accuracy on demand, but also and foremost to enable localization feasibility in harsh operating contexts or under limited deployment settings for which conventional systems based on active BSs would fail [4], [5]. For instance, RRISs have already been considered for parametric multipath-aided positioning in both LoS (e.g., [6]–[10]) or NLoS (e.g., [11]–[13]) conditions, encompassing far and near field propagation regimes. However, most of these state-of-the-art contributions are still based on simplistic models and synthetic simulations for performance evaluation.

In contrast, this paper accounts for preliminary proof-of-concept validations of RIS-aided positioning in a single-BS indoor scenario, relying on frequency-domain mmWave



Fig. 1: Picture of the indoor environment and equipment considered for the mmWave measurement campaign.

channel measurement data. The main paper contributions can be summarized as follows: (i) we describe a dedicated Vector Network Analyzer (VNA)-based channel measurement campaign, which was carried out with real RRIS [14] and Transmit RIS (TRIS) [15] prototypes, both with beamforming capabilities, as well as a monopole antenna mounted on a positioner enabling high-resolution multipath estimation; (ii) we conduct an analysis of the RIS-reflected multipath components in terms of delay, Angle of Arrival (AoA) and AoD (i.e., beyond overall channel gains) in light of localization needs; (iii) we benchmark positioning results for several UE and RRIS locations, while considering various combinations of estimated multipath parameters or overall channel parameters; (iv) we illustrate concrete limitations related to the presence of grating lobes at the RRIS and/or too large distances between the RRIS and the UE. To the best of our knowledge, these experiments represent a world premiere demonstrating the validity of the RIS-aided localization concept at mmWave frequencies based on a real-life surface prototype.

II. MMWAVE CHANNEL MEASUREMENTS

A. Experimental Setup and Measurement Procedure

The experimental setup committed in our measurement campaign relies on a VNA-based mmWave channel sounder, which is similar to that used in [16]. It includes a TRIS [15] on the transmitter (TX) side and a RRIS [14] between the TX and the receiver (RX), both with 1-bit element-wise phase control. In the following descriptions, unless specified, we reserve the term “RIS” to the reflective RIS, while systematically

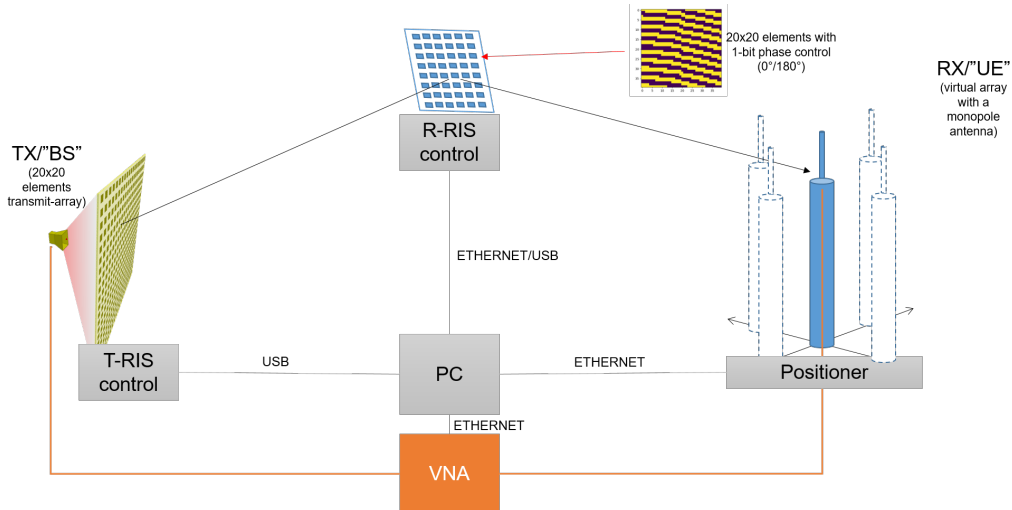


Fig. 2: Simplified block diagram of the RIS-enabled mmWave VNA-based channel sounder, with 1-bit RRIS phase control.

depicting the TRIS as "BS" for the sake of simplicity. Fig. 2 shows a simplified block diagram of the overall measurement acquisition chain. Both the floor plan of the reference indoor environment and the tested deployment configurations are represented in Fig. 3. Lying in a unique reference location for all the tested configurations, the BS first performed a beam scanning in azimuth from -60° to $+60^\circ$, by a step of 5° , while the RRIS was still off. Then, using a static beam, the BS just illuminated the activated RRIS, which was tested sequentially within two distinct location/orientation configurations. For each location/orientation setting, the RRIS was controlled through a codebook to perform also beam sweeping in azimuth from -60° to $+60^\circ$, still by the same step of 5° . For the scanning process of both BS and RRIS, a unique anticlockwise convention was used to define the AoDs, using a reference angle (i.e., 0°) normal to the surface/array. The measurement procedure above was repeated over 5 main UE positions. In each of those positions, the RX monopole antenna was moved over a 3×3 small-scale grid (i.e., considering a virtual square array in the horizontal x - y plane) thanks to a high-precision positioner, and a frequency-domain complex channel response between the TX and the RX was recorded from 25 to 35 GHz by the step of 10 MHz on each occupied small-scale position, although a bandwidth of 2 GHz (among the measured 10 GHz bandwidth) was further used in practice in our localization tests (See Sec. II-B) to emulate the behaviour of a realistic receiver. Note that the three involved entities (i.e., BS, RRIS and UE) were all set at the same height of 1.6m and hence, lying on the same 2D plane during all experiments.

B. Measurement Data Calibration and Pre-processing

The effect of all cables and RF components in the acquisition chain was pre-characterized and calibrated out of all the recorded complex frequency-domain channel responses. Then, thanks to the virtual 3×3 array used at the RX UE, for each tested location and pointing beam direction (at the BS or the RRIS), the classical high-resolution Space-Alternating Generalized Expectation-maximization (SAGE) algorithm [17]

was applied to extract the parameters of the most significant multipath components (MPCs), including the travelled Over-the-Air (OTA) distance (or equivalently, the delay¹), and the AoA and the gain. For this extraction, as a stopping rule, we have considered retrieving up to 99% of the total channel energy, with a limitation to the 20 strongest MPCs. SAGE was applied to a 2GHz sub-band centered around the RRIS operating frequency, that is, between 27 and 29 GHz. In the following analysis, among all the MPCs extracted by SAGE, both the BS-UE direct path (whenever available) and the BS-RRIS-UE reflected path were isolated² using the expected geometric information in terms of travelled distance and AoA (i.e., performing genie-aided space-time filtering), while the overall channel gain was computed out of the gains of all the resolved MPCs.

III. RADIO FEATURES AND POSITIONING

A. Location-dependent Radio Features

Picking up the maximum values taken by the overall channel gain over all possible beam pointing directions (i.e., in azimuth, discretized by steps of 5°), we first come up with coarse AoD estimates, $\tilde{\varphi}_{BS}$ and $\tilde{\varphi}_{RIS}$, respectively after BS and RRIS beam sweepings. Likewise, based on MPCs extraction, we also consider fine AoD estimates, based on the three maximum values taken by the gains of isolated MPCs (i.e., the DP or a

¹As we operate with a VNA, TX-RX synchronization is inherently solved and any estimated delay directly coincides with the absolute time of flight, after calibration. In a real asynchronous system relying on relative delay estimation at the RX though, either multi-way protocol exchanges, or joint localization and synchronization algorithms [10], would be necessary.

²Focusing mostly on effects such as signal-to-noise ratio or geometry in our analysis, the detection of a so-called *isolated* MPC is herein idealized for simplicity. It is genie-aided in the sense that we are interested only in the MPCs extracted in a distance-AoA region where the geometric path (i.e., the Direct Path (DP) or a RIS Reflected Path (RP)) is expected to lie within an arbitrary tolerance margin of $\pm 1m$ in terms of travelled OTA distance and $\pm 15^\circ$ in terms of AoA (See the black circles in Fig. 4). In turn, more advanced processing would be necessary to isolate those contributions (typically, after subtracting all the static contributions from non-RIS MPCs out of channel responses), while in a real dynamic system, further processing such as filtering could be applied to leverage prior information about the UE location.

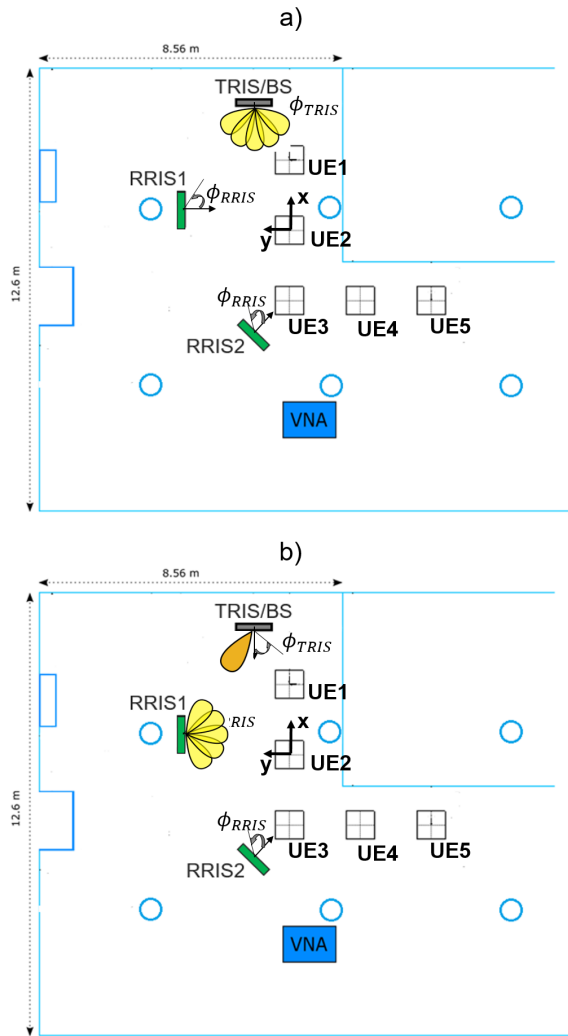


Fig. 3: Layout and deployment considered in the mmWave channel measurement campaign, including 1 BS location, 2 RRIS locations (RRIS1 and 2) and 5 UE locations (UE1 to UE5), represented for both the BS and RRIS1 beams sweeping phases (resp. a and b).

RIS RP) over all possible pointing directions, after performing BS and RRIS beam sweeping. Fig. 5 and 6 show examples of such AoD estimation with respect to the first UE location (i.e., UE1), respectively for DP after BS beam scanning and for RP after beam RRIS scanning (for two distinct RRIS locations). In this illustration, $\tilde{\phi}_{BS} = 30.0^\circ$ for a ground-truth angle of 32.0° (See Fig. 5), while $\tilde{\phi}_{RRIS1} = 25^\circ/0^\circ/30^\circ$ for a ground-truth angle of 24.6° (See Fig. 6 - left) and $\tilde{\phi}_{RRIS2} = 0^\circ/35^\circ/10^\circ$ for a ground-truth angle of 31.9° (See Fig. 6 - right).

Besides, calibrated delays (or equivalently, OTA traveled distances) associated with the same isolated MPCs have also been considered to complete angular estimates in some positioning scenarios (See Sec. III-B).

Finally, estimated AoAs are herein used for spatially filtering out the MPCs of interest, although they could be used also for UE orientation estimation, which falls out of the scope of this paper.

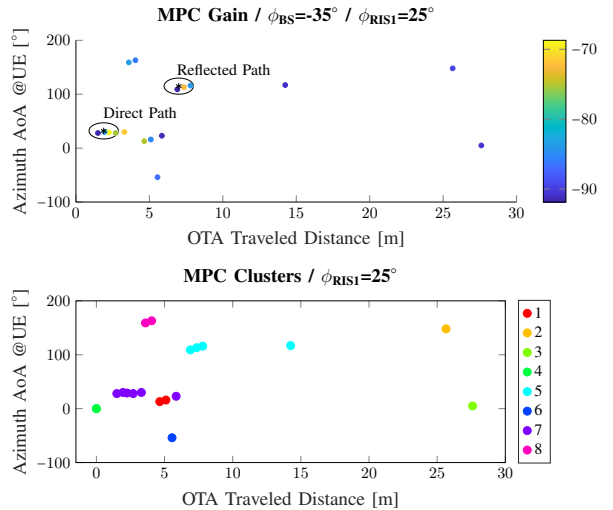


Fig. 4: Example of scatter plot of extracted MPC gains (in dB) as a function of both their AoAs (in $^\circ$) and traveled OTA distances (in m) (top), along with the corresponding MPC clusters (bottom), for the BS beam pointing to the first RRIS location (i.e., $\phi_{BS} = -35^\circ$) and the same RRIS pointing to the first UE location (i.e., $\phi_{RRIS1} = 25^\circ$).

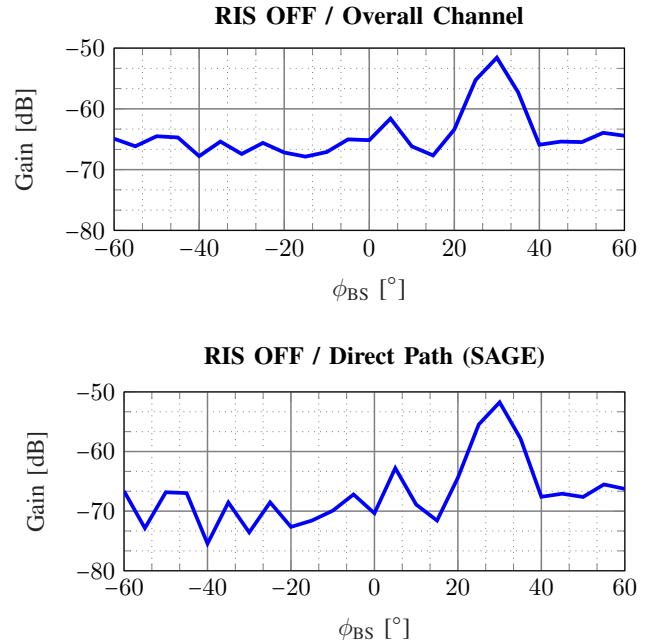


Fig. 5: Overall channel (top) and DP (bottom) gains in the first tested location (UE1) after BS beam scanning, as a function of ϕ_{BS} , with the RRIS off.

B. Positioning Scenarios and Method

In all the tested positioning configurations, we assume that both the positions and the orientations of BS and/or RRIS are perfectly known. Table I summarizes the corresponding scenarios, depending on the combination of location-dependent radio features extracted from channel responses, as well as the expected benefits from using RIS on top a conventional single-BS system (i.e., either enabling or boosting localization).

In a real system, from a protocol standpoint, the scenarios making use of several MPCs (i.e., all except 0, 2d and 2e)

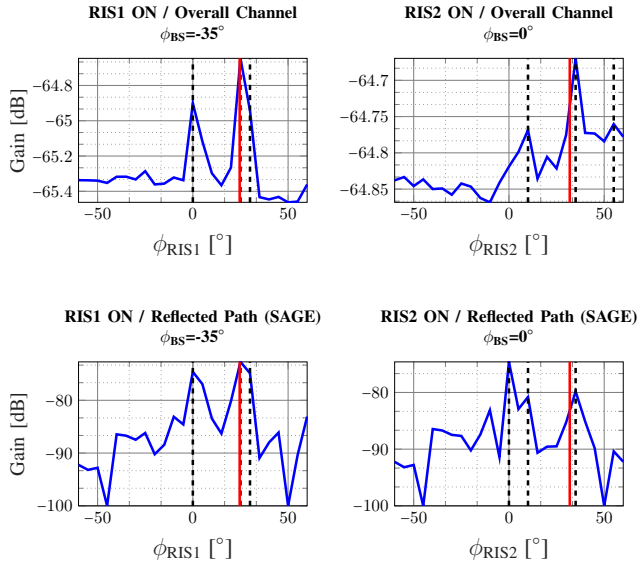


Fig. 6: Overall channel (top) and RP (bottom) gains in first position (UE) after RRIS beam scanning, as a function of ϕ_{RIS1} with $\phi_{BS} = -35^\circ$ (left) or ϕ_{RIS2} with $\phi_{BS} = 0^\circ$ (right), with its Ground-Truth angle (solid red) and the corresponding 3 strongest candidate estimates (dashed black)

would necessitate a sequential illumination sequence from the BS (e.g., BS beam scanning first whenever DP is used and/or RISs beam scanning under static BS beam), coming up with one set of estimated location-dependent radio parameters for each BS pointing direction, which need to be recombined offline for positioning. In all these multipath scenarios, for the purpose of fair comparisons and putting more emphasis on the impact of radio parameters estimation, positioning is systematically determined through standard non-linear LS optimization, initialized with the same random guess (drawn in the entire tested indoor area) and fed by the best candidate AoD angles. In a real system, the latter optimistic assumption could be relaxed by leveraging prior knowledge of the RIS beam patterns (as a function of the impinging angle) and/or the output of a tracking filter in case of dynamic scenario (i.e., both previous UE estimates and its related uncertainty).

Other positioning approaches could have been considered too, such as that relying on weighted combinations of the received powers (or power gains in our case) over a grid of possible UE candidate locations (e.g., [4]), hence guaranteeing more homogeneous 2D spatial resolution regardless to the RIS-UE distance. However, the latter method would have required the prior discretization of the 2D Cartesian space during measurements collection and the pre-calculation of BS and RRIS beams accordingly, rather than the simpler azimuth domain discretization imposed here.

IV. RESULTS

A. Radio Parameters Estimation

Fig. 7 and 8 show estimation errors respectively for RIS AoDs and the overall OTA distances travelled by RIS-reflected paths (i.e., from BS to UE, through the RRIS), both as a function of the true RIS-UE distance (i.e., over the 5 UE locations and the 2 RIS locations). For AoDs first, we show

the errors corresponding to the 3 maximum values taken by overall channel gains (top) or SAGE MPC gains (bottom) over all possible azimuth angles, along with the best choice (among these 3 candidates). As expected, one can observe that the AoD error globally increases with the RIS-UE distance, staying typically below 5° (i.e., within the azimuth discretization step) at distances up to 5m but growing to several tens of degrees for distances beyond 5m, even in the best case. Whatever the RIS location, the same trends are globally observed with the two estimation methods, which anyway lead roughly to the same estimates in a majority of tested cases. Nevertheless, the use of MPC gains seems to outperform that of overall channel gains at larger RIS-UE distances (typically with errors up to 14.7° and 70.3° , respectively, at 7.5m from the first RIS). This is likely due to the fact that, at larger RIS-UE distances, the dynamics of the overall channel gain as a function of RIS AoD is relatively limited and hence, more challenging to interpret. Both approaches suffer similarly from the presence of strong grating lobes in the RIS beam patterns, which tends to generate local maxima (at wrong AoD angles, possibly very distant from the ground-truth) in both channel and reflected path gains, even at short distances (See Fig. 6). It shall be also noted that the angular step of 5° applied for beam scanning is quite large compared to the RRIS -3dB beamwidth (i.e., below 3° for the considered prototype [14]). This effect contributes to the fact that some grating lobes could contribute even more than the apparent main lobe. Accordingly, the angle leading to the strongest power gains does not even always coincide with the best candidate. Regarding the distance estimation of RIS-reflected paths, on Fig. 8, the negative influence of the RIS-UE distance looks less obvious than for AoD estimation. The latter is thus expected to be the dominating factor with respect to positioning performance in our evaluations.

B. 2D Position Estimation

Fig. 9 illustrates, qualitatively, the positioning results for 4 of the 5 tested UE locations and the 11 scenarios of Table I, while Table II reports, quantitatively, the corresponding errors per UE location, along with the sample median error and Root Mean Square Error (RMSE) (both calculated over the 5 UE tested locations). In this table, the symbol \downarrow indicates that the error is significantly higher than the best result, typically according to Wilcoxon's rank sum test used at the p -value threshold of 0.01 [18]. The latter entries correspond mostly to test configurations where the RP1 is used at large RIS-UE distances, typically with respect to UE5 locations and, to a minor extent, with respect to UE4. First, this is in line with the link-level radio parameters estimation results in Sec. IV-A, where AoD estimation errors can typically exceed 10° as RIS-UE distances reach 5m-6m, whatever the estimation method. Beyond, regardless of the quality of radio parameters estimation, due to the 5° AoD discretization step used for beam sweeping in azimuth, positioning errors naturally tend to be larger at large distances, due to obvious geometric dilution considerations.

TABLE I: Positioning scenarios as a function of combined radio metrics.

Scenario	MPCs [Nb R-RISs]	LoS/NLoS Status	Radio Metrics [Method]	Expected RIS Benefits
0	DP only [0 R-RIS]	LoS	$\tilde{\phi}_{BS}, \tilde{d}_{DP}$ [SAGE MPCs]	N/A (Baseline)
1a	DP + RP1 [1 R-RIS]	LoS	$\tilde{\phi}_{BS}, \tilde{\phi}_{RIS1}$ [Overall Channel Gain]	Enabled localization*
1b	DP + RP2 [1 R-RIS]	LoS	$\tilde{\phi}_{BS}, \tilde{\phi}_{RIS2}$ [Overall Channel Gain]	Enabled localization*
1c	DP + RP1 + RP2 [2 R-RISs]	LoS	$\tilde{\phi}_{BS}, \tilde{\phi}_{RIS1}, \tilde{\phi}_{RIS2}$ [Overall Channel Gain]	Enabled localization*
1d	RP1 + RP2 [2 R-RISs]	NLoS	$\tilde{\phi}_{RIS1}, \tilde{\phi}_{RIS2}$ [Overall Channel Gain]	Enabled localization*
2a	DP + RP1 [1 R-RIS]	LoS	$\tilde{\phi}_{BS}, \tilde{d}_{DP}, \tilde{\phi}_{RIS1}, \tilde{d}_{RP1}$ [SAGE MPCs]	Boosted localization**
2b	DP + RP2 [1 R-RIS]	LoS	$\tilde{\phi}_{BS}, \tilde{d}_{DP}, \tilde{\phi}_{RIS2}, \tilde{d}_{RP2}$ [SAGE MPCs]	Boosted localization**
2c	DP + RP1 + RP2 [2 R-RISs]	LoS	$\tilde{\phi}_{BS}, \tilde{d}_{DP}, \tilde{\phi}_{RIS1}, \tilde{d}_{RP1}, \tilde{\phi}_{RIS2}, \tilde{d}_{RP2}$ [SAGE MPCs]	Boosted localization**
2d	RP1 [1 R-RIS]	NLoS	$\tilde{\phi}_{RIS1}, \tilde{d}_{RP1}$ [SAGE MPCs]	Enabled localization***
2e	RP2 [1 R-RIS]	NLoS	$\tilde{\phi}_{RIS2}, \tilde{d}_{RP2}$ [SAGE MPCs]	Enabled localization***
2f	RP1 + RP2 [2 R-RISs]	NLoS	$\tilde{\phi}_{RIS1}, \tilde{d}_{RP1}, \tilde{\phi}_{RIS2}, \tilde{d}_{RP2}$ [SAGE MPCs]	Enabled localization***

* Vs. conventional single-BS positioning using also RSS measurements (i.e., missing additional links wrt. other BSs).

** Vs. conventional single-BS positioning with similar MPCs estimation capabilities, but relying on DP only (See Scenario 0).

*** Vs. conventional single-BS positioning with similar MPCs estimation capabilities, but relying on DP only (i.e., missing additional LoS links wrt. additional BSs), or with no extra Simultaneous Localization And Mapping (SLAM) capabilities (i.e., unable to position scatterers out of the extracted MPCs, jointly with UE).

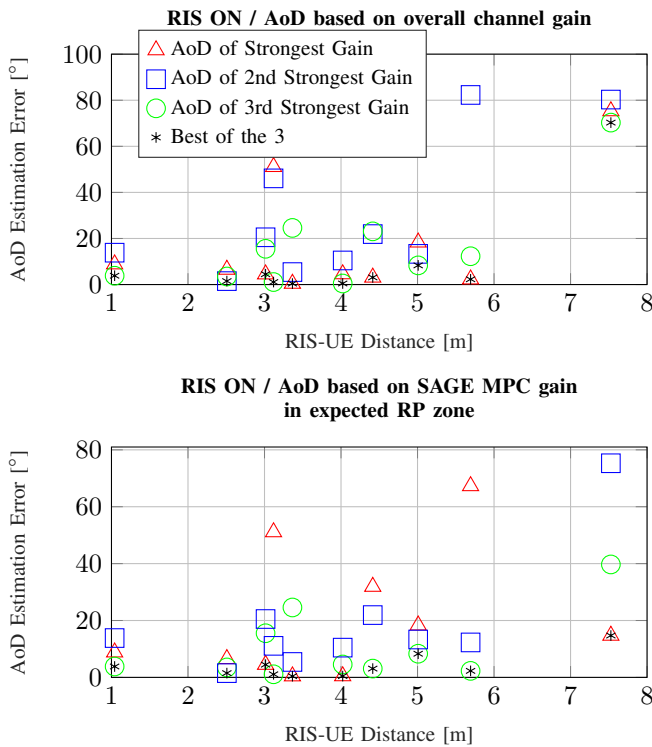


Fig. 7: RIS AoD estimation errors, as a function of the true RIS-UE distance, relying on 3 maximum values taken by overall channel gain (top) or SAGE MPCs gain (bottom), over all RRIS and UE locations.

Nevertheless, it is also observed that despite the use of poorly informative radiolocation metrics such as that related to received power (herein, BS and RIS AoDs based on overall channel gain), single-BS still seems feasible in Scenarios 1a to 1c within an accuracy level comparable to that of the reference scenario 0. Mitigating a little bit the previous result, it should be recalled that channel sounding equipment usually benefits from better signal dynamics and sensibility than that

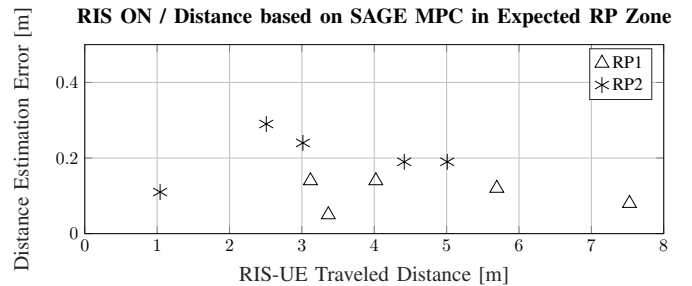


Fig. 8: Multipath distance estimation errors, as a function of the true RIS-UE distance for reflected paths RP1 and RP2, over all RRIS and UE locations.

TABLE II: LS positioning errors (in m) for the scenarios of Table I.

Scenario	UE1	UE2	UE3	UE4	UE5	RMSE	Median
0	0.09	0.04	0.01	0.21	0.22	0.15	0.09
1a	0.07	0.09	0.06	0.84↓	7.16↓	3.22↓	0.08
1b	0.30	0.15	0.07	0.48	0.83↓	0.46	0.30
1c	0.11	0.05	0.07	0.39	2.99↓	1.35↓	0.11
1d	0.27	0.10	0.07	0.24	6.78↓	3.04↓	0.24
2a	0.02	0.06	0.07	0.24	1.40↓	0.64↓	0.07
2b	0.18	0.13	0.06	0.28	0.44	0.25	0.18
2c	0.12	0.13	0.07	0.27	0.97↓	0.46	0.13
2d	0.05	0.15	0.14	0.26	2.60↓	1.17↓	0.16
2e	0.42	0.30	0.13	0.34	0.76	0.44	0.34
2f	0.22	0.22	0.11	0.30	1.35↓	0.63↓	0.22

of integrated receivers at real UE terminals. Accordingly, the latter may be subject to relatively large fluctuations of the received power (in comparison with the power gain brought by RIS reflections), hence making the detection of RIS AoDs more challenging in practice.

Finally, as regards to the expected localization boost, none of the tested RIS-aided configurations (in terms of both radio metrics or UE locations) could really outperform this reference scenario, suggesting that passive RRIS are most likely beneficial to enable non-feasible localization configurations, rather than improving localization accuracy.

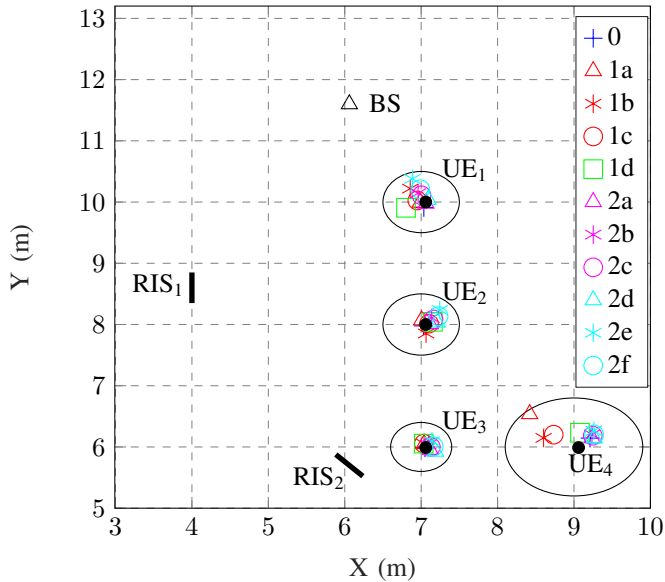


Fig. 9: Ground-truth and estimated UE locations (over the 4 first tested locations) for the scenarios of Table I.

V. CONCLUSION AND FUTURE WORK

In this paper, we account for first experimental validations of RIS-aided single-BS positioning based on real frequency domain mmWave channel sounding measurements. Basic LS positioning results show that the AoDs of 2 RIS-reflected paths (or even the AoD and delay of 1 single RIS-reflected path) could viably (i) replace the missing direct path in case of NLoS situation between the BS and the UE or (ii) complete this direct path in LoS, both given that the RIS-UE distance remains on the order of a few meters at most. Beyond, it is noted that the estimation of RIS-reflected path parameters could be significantly degraded, thus making counterproductive RIS contribution to the final positioning result.

Leveraging the same measurement data, future works will investigate the impact of bandwidth occupancy on performance, as well as the suppression of the systematic static multipath components to ease the detection of RIS-reflected paths, hence getting rid of the genie-aided spatial pre-filtering step in the Delay-AoA domain. Other possible RIS-based applications in the same context concern the localization of passive objects for opportunistic mapping purposes.

ACKNOWLEDGMENT

This work has been supported, in part, by the EU H2020 RISE-6G project under grant 101017011. The authors would also like to warmly thank J.-B. Gros from Greenerwave, for

providing the RRIS prototype involved in the measurement campaign reported here, as well as for his technical assistance and meaningful advice.

REFERENCES

- [1] C. Huang et al, "Reconfigurable Intelligent Surfaces for Energy Efficiency in Wireless Communication," *IEEE Trans. Wireless Commun.*, vol. 18, pp. 4157–4170, Aug. 2019.
- [2] Q. Wu and R. Zhang, "Intelligent reflecting surface enhanced wireless network via joint active and passive beamforming," *IEEE Trans. Wireless Commun.*, vol. 18, pp. 5394–5409, Nov. 2019.
- [3] E. Calvanese Strinati, G. C. Alexandropoulos, H. Wymeersch, B. Denis, V. Sciancalepore, R. D'Errico, A. Clemente, D.-T. Phan-Huy, E. D. Carvalho, and P. Popovski, "Reconfigurable, intelligent, and sustainable wireless environments for 6G smart connectivity," *IEEE Commun. Mag.*, vol. 59, pp. 99–105, Oct. 2021.
- [4] K. Keykhosravi et al., "Leveraging RIS-Enabled Smart Signal Propagation for Solving Infeasible Localization Problems," 2022.
- [5] H. Wymeersch et al., "Radio localization and mapping with reconfigurable intelligent surfaces: Challenges, opportunities, and research directions," *IEEE Vehicular Technology Magazine*, vol. 15, no. 4, pp. 52–61, 2020.
- [6] H. Wymeersch and B. Denis, "Beyond 5G Wireless Localization with Reconfigurable Intelligent Surfaces," in *ICC 2020 - 2020 IEEE International Conference on Communications (ICC)*, (Dublin, Ireland), pp. 1–6, IEEE, June 2020.
- [7] A. Elzanaty et al., "Reconfigurable intelligent surfaces for localization: Position and orientation error bounds," *IEEE Transactions on Signal Processing*, vol. 69, pp. 5386–5402, 2021.
- [8] J. He, H. Wymeersch, L. Kong, O. Silvén, and M. Juntti, "Large intelligent surface for positioning in millimeter wave mimo systems," in *2020 IEEE 91st Vehicular Technology Conference (VTC2020-Spring)*, pp. 1–5, 2020.
- [9] H. Zhang, H. Zhang, B. Di, K. Bian, Z. Han, and L. Song, "Towards ubiquitous positioning by leveraging reconfigurable intelligent surface," *IEEE Communications Letters*, vol. 25, no. 1, pp. 284–288, 2021.
- [10] K. Keykhosravi et al., "SISO RIS-enabled joint 3D downlink localization and synchronization," in *Proc. IEEE ICC*, (Montreal, Canada), 2021.
- [11] M. Rahal et al., "RIS-enabled localization continuity under near-field conditions," in *Proc. IEEE SPAWC*, (Lucca, Italy), 2021.
- [12] M. Rahal, B. Denis, K. Keykhosravi, M. F. Keskin, B. Uguen, and H. Wymeersch, "Constrained ris phase profile optimization and time sharing for near-field localization," in *2022 IEEE 95th Vehicular Technology Conference: (VTC2022-Spring)*, pp. 1–6, 2022.
- [13] Y. Liu, E. Liu, and R. Wang, "Reconfigurable Intelligent Surface Aided Wireless Localization," *arXiv:2009.07459 [cs, math]*, Sept. 2020. arXiv: 2009.07459.
- [14] J.-B. Gros et al., "A reconfigurable intelligent surface at mmwave based on a binary phase tunable metasurface," *IEEE Open Journal of the Communications Society*, vol. 2, pp. 1055–1064, 2021.
- [15] L. Di Palma et al., "1-Bit Reconfigurable Unit Cell for Ka-Band Transmitarrays," *IEEE Antennas and Wireless Propagation Letters*, vol. 15, pp. 560–563, 2016.
- [16] T. Mazloum et al., "Impact of Multiple RIS on Channel Characteristics: An Experimental Validation in Ka Band," in *Proc. 2023 Joint European Conference on Networks and Communications & 6G summit (EuCNC/6G summit)*, June 2023.
- [17] K. Haneda and J.-I. Takada, "An application of SAGE algorithm for UWB propagation channel estimation," in *Proc. IEEE Conference on Ultra Wideband Systems and Technologies 2003 (IEEE UWBST'03)*, pp. 483–487, November 2003.
- [18] F. Wilcoxon, "Individual comparisons by ranking methods," *Biometrics*, vol. 1, no. 6, pp. 80–83, 1945.